Focus latitude enhancement of symmetrical phase mask design for deep submicron contact hole patterning

Shuo-Yen Chou, Jen-Chung Lou, Li-Jui Chen, Lin-Hung Shiu, Ru-Gun Liu, Chien-Ming Wang, and Tsai-Sheng Gau

Focus latitude enhancement of symmetrical phase mask design for deep submicron contact hole patterning

Shuo-Yen Chou[a)] and Jen-Chung Lou
Department of Electronics Engineering and Institute of Electronics, National Chiao-Tung University, Hsinchu, Taiwan 30050, Republic of China

Li-Jui Chen, Lin-Hung Shiu, Ru-Gun Liu, Chien-Ming Wang, and Tsai-Sheng Gau
Deep Sub-micron Technology Division, Electronics Research & Service Organization, Industrial Technology Research Institute, Chutung, Hsinchu, Taiwan 310, Republic of China

The mechanism of focus latitude enhancement for contact/via hole printing is explained by approximating the axis intensity distribution of an image as a series of cosine functions to characterize the interference between each pair of diffraction beams. It is found that a phase-shifting mask (PSM) with symmetrical assist features improves the depth of focus (DOF) by introducing destructive interference to counterbalance the intensity fluctuation from constructive interference as defocus. A simple formula was derived to represent the capability of focus latitude enlargement. It shows that the extent of enhancement depends on the exposure wavelength and numerical aperture of a projection lens only. Increasing the degree of partial coherence degrades the focal range enlargement because a larger illumination angle elongates the destructive interference pattern in the optical-axis direction to weaken its ability for intensity compensation. On the other hand, the lack of constructive interference in dense hole imaging fails the mask pattern transfer, which limits the application of the phase-shifting method to pattern pitch greater than $\sqrt{2}\lambda/\mathrm{NA}$. A tiny amount of spherical aberration results in prominent asymmetrical defocus behavior because the wave deformation in the projection lens shifts the distribution of constructive and destructive interference patterns to opposite defocus directions. The printing characteristics of 0.17 μm contact using an 18% transmission, rim-type attenuated phase-shifting mask are investigated to corroborate our analysis of defocus behavior. The dependence of depth of focus on pattern duty is stressed to elucidate the difference in mechanisms of focus latitude improvements for a sparse hole and periodic dense hole. © *2001 American Vacuum Society.* [DOI: 10.1116/1.1418398]

I. INTRODUCTION

Large depth of focus (DOF) is required in projection optical lithography to overcome the process issues like uneven surface of a device and focus adjustment error. Phase-shifting mask[1,2] (PSM) is a popular superresolution technique to retain relatively large DOF while increasing the numerical aperture (NA) for higher resolution capability at a fixed wavelength. For contact-hole printing, the PSMs often have symmetrical phase-shifted assist features surrounding the main feature opening. Outrigger design in Levenson-type PSMs and rim-shifter design with different transmission in attenuated PSMs have been applied to deep submicron contact-hole printing using today's workhorse 248-nm machines.[3-6] As explained by Schellenberg[7] and Socha,[8] the contact PSM design is based on the principle of approximating the mask function to a Bessel function, which has a transverse electric field independent of the propagation distance, and thus significantly improves the DOF. However, this coarse approximation is inconclusive for correlating the defocus behavior with the optical system parameters and mask variables. As the optical condition varies, tedious simulation work must be done to reoptimize mask parameters for satisfactory lithographic performance.

In this article we thoroughly explained the working principle of symmetrical phase-mask design for contact hole patterning by projection optics. The correlation between focus latitude enhancement and optical system parameters was analyzed. A simple formula was derived as a metric to represent the capability of DOF enlargement. We also elucidated the effect of illumination angle, pattern pitch restriction, and influence of spherical aberration on DOF improvement for real process applications. To verify our analysis, an 18% transmission rim-type attenuated PSM was employed in 0.17 μm contact-hole printing, which corresponds to a low k_1 factor of 0.38 in our exposure system. The lithographic performances of a variety of contact features with different rim widths and array pitches were evaluated under conventional and purely off-axis illuminations. The dependence of DOF on pattern pitch is confirmed experimentally. Possible approaches to remedying the inability of this superresolution technique for dense hole printing are also discussed.

II. MECHANISM OF DEPTH OF FOCUS ENHANCEMENT

Figure 1 shows the schematic view of image formation by a projection lens. In Fourier optics, the calculation of amplitude distribution in the ideal image plane $U_i(x,y)$ starts with a Fourier transform of the complex amplitude of the mask
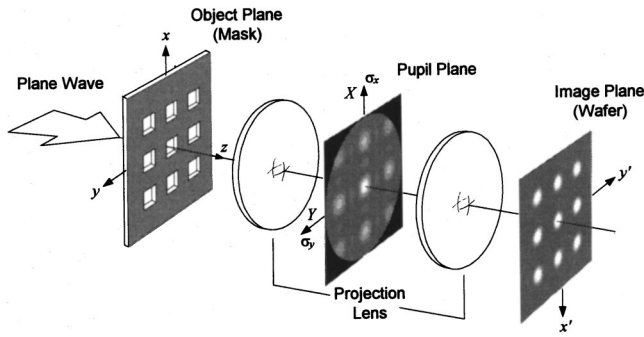

FIG. 1. Schematic view of coherent image formation by the projection lens system.

'function, $U_m(x,y)$, proceeds with calculating the propagation of the Fourier components in the optical system, and ends with an inverse Fourier transform.[9] With the consideration of defocus effect, since the focal length is sufficiently large compared with the wavelength λ of light to validate the application of stationary-phase approximation,[10] the three-dimensional amplitude distribution of image in the vicinity of the focal point can be expressed as follows:

$$U_i(x',y',d) = F^{-1}\left[F\{U_m(x,y)\}\mathrm{circ}(\sqrt{\sigma_x^2+\sigma_y^2}/\mathrm{NA}) \right.$$
$$\left. \times \exp\left(i\frac{2\pi}{\lambda} d\sqrt{1-(\sigma_x^2+\sigma_y^2)} \right) \right]. \tag{1}$$

Here σ_x and σ_y are the direction cosine of the plane waves. F and F^{-1} denote a Fourier transform and an inverse Fourier transform, respectively. The variable d specifies the defocus distance from the ideal image point. The circle function circ represents the pupil function of the projection system. The defocus behavior of image is determined by the complex exponential term in Eq. (1).

The Fourier transform in Eq. (1) is generally calculated by a computer by representing the complex exponential term in the $\sigma_x\sigma_y$ plane using a discrete mesh with a reasonable number of samples. A similar sampling process occurs at the pupil plane when the mask patterns are arranged in a repetitive array, which gives a discrete Fourier spectrum composed of various diffraction-order beams. Since regular arrays of holes are general in large-scale integration (LSI) layout and often used as test patterns to evaluate the lithographic performance, we assumed the pattern in the mask plane is a periodic hole array with pitch p in both x and y directions so that the object spectrum at the pupil becomes a dot array with a pitch of λ/p. Let f_{mn} denote the complex amplitude of (m,n)-order diffraction light. The Fourier transform in Eq. (1) could be rewritten in the form of a double trigonometric series,[11] and the amplitude distribution of the image is expressed as follows:

$$U_i(x,y,d)$$
$$= \sum_{m,n=0}^{\sqrt{m^2+n^2}\leqslant p\mathrm{NA}/\lambda} \alpha_{mn}f_{mn}\cos\left(2\pi x\frac{m}{p}\right)\cos\left(2\pi y\frac{n}{p}\right)$$
$$\times \exp\left(i2\pi\frac{d}{\lambda}\sqrt{1-(m^2+n^2)(\lambda/p)^2} \right), \tag{2}$$

where

$$\alpha_{mn} = 2^{2-\delta(m)-\delta(n)}, \quad \text{with } m,n \geqslant 0.$$

Since defocus accompanies the loss of intensity at the center of the image patch, we observed the central intensity variation of an image spot to characterize the defocus behavior. Calculating the square of Eq. (2) and letting $x,y=0$, we obtained the central intensity distribution with the form

$$I_c(d) = \sum_{m,n=0}^{\sqrt{m^2+n^2}\leqslant p\mathrm{NA}/\lambda} \sum_{u,v=0}^{\sqrt{u^2+v^2}\leqslant p\mathrm{NA}/\lambda} \alpha'_{mnuv}f_{mn}f_{uv}$$
$$\times \cos[2\pi(d/\lambda)(\sqrt{1-(m^2+n^2)(\lambda/p)^2}$$
$$- \sqrt{1-(u^2+v^2)(\lambda/p)^2})], \tag{3}$$

where

$$\alpha'_{mnuv} = 2^{4-\delta(m)-\delta(n)-\delta(u)-\delta(v)}, \quad \text{with } m,n,u,v \geqslant 0.$$

In Eq. (3) the exponential term related to defocus behavior is transformed into a cosine function. The period of each cosine function is inversely proportional to the difference in the z component of the propagation vector between the two interacted diffraction beams. For an isolated contact feature with continuous diffraction spectrum at the pupil, its defocus behavior can be accurately approximated by a series of cosine functions with a reasonable large array pitch for sufficient sampling points at the pupil. To reduce the redundant cosine functions in Eq. (3) for a clear and simple illustration of defocus behavior, we choose a coarse mesh with only nine sampling points to represent the pupil [see Fig. 2(a)]. This corresponds to the case in which the pitch of the contact array is so small that the projection-lens pupil samples only nine diffraction orders. Consequently, the central intensity distribution of Eq. (3) reduces to

$$I_c(d) = f_{00}^2 + 16f_{(10)}^2 + 16f_{11}^2 + 8f_{00}f_{(10)}$$
$$\times \cos[2\pi(d/\lambda)(1-\sqrt{1-(\lambda/p)^2})] + 8f_{00}f_{11}$$
$$\times \cos[2\pi(d/\lambda)(1-\sqrt{1-2(\lambda/p)^2})] \tag{4}$$
$$+ 32f_{(10)}f_{11}\cos[2\pi(d/\lambda)(\sqrt{1-(\lambda/p)^2}$$
$$- \sqrt{1-2(\lambda/p)^2})],$$

where $f_{(10)}$ equals f_{10} and f_{01}.

Since an aperture near or smaller than the wavelength diffracts light to fill the pupil almost uniformly, we assume all the diffraction beams collected by the pupil have an amplitude equal to unity to simplify calculation. Equation (4) was graphed in Fig. 2(b) with the optical condition of $\lambda=248$ nm and NA=0.55. The pattern pitch is 1.78 λ/NA for con-
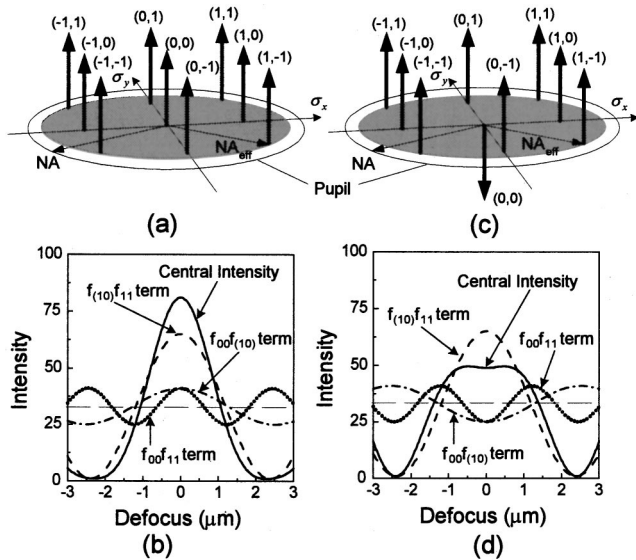
FIG. 2. Sampling the pupil by a coarse mesh with nine data points. (a) Conventional method with all diffraction orders in phase, and (b) the corresponding central intensity distribution. (c) Phase-shifting method with the zeroth-order diffraction beam 180° out of phase, and (d) the corresponding central intensity distribution.

forming the nine-beam-interference condition. Every cosine term in Eq. (4) (plus the dc values: $f_{00} + 16f_{(10)} + 16f_{11}$) is also plotted in this figure to demonstrate the interference between each pair of diffraction orders. Since the diffraction beams with indices of $(0,0)$, $(\pm 1,0)$, $(0,\pm 1)$, and $(\pm 1,\pm 1)$ are all in phase, the cosine functions with coefficients $f_{00}f_{(10)}, f_{00}f_{11}$, and $f_{(10)}f_{11}$ have synchronized distribution near the ideal image point. Thus the central intensity I_c declines rapidly as defocus, which implies a small focus latitude.

Figure 2(b) indicates possible approaches to improving the focus latitude. Regardless of the image fidelity in wafer plane, the most effective method is eliminating all cosine terms that originate intensity fluctuation as defocus in Eq. (4). This method can be fulfilled by inserting a thin annular aperture at the pupil plane so that only the diffraction elements with radial position equal to the radius of the annulus are collected. Theoretically speaking, this method generates a nondiffraction field with the form of Bessel functions in the image plane to provide infinite DOF.[12,13] However, a finite width of the annular aperture is required either to cover a wide range of pitch values or to let sufficient power transmit through the pupil to expose the photoresist.[14] Consider an annular aperture with finite width that blocks the central order but let the other eight diffraction orders in Fig.2(a) pass; the resulting central intensity profile is determined by the $f_{(10)}f_{11}$ term only. Refer to Fig. 2(b), the $f_{(10)}f_{11}$ term has less steep intensity variation then the superposed intensity I_c, which indicates a larger defocus tolerance than that without annular aperture. However, this enhancement is insufficient when the target critical dimension (CD) is so small that a tiny amount of intensity variation results in large consumption of the CD budget. A flatter central intensity distribution

is required to maintain sufficient DOF as CD decreases.

Another more feasible method with full pupil utilization is reversing the distribution of some of the cosine terms to retard the intensity loss as defocus. This method can be fulfilled by shifting the phase of the zeroth-order diffraction beam by π to reverse the distribution of cosine terms $f_{00}f_{(10)}$ and $f_{00}f_{11}$ [see Fig. 2(c)]. The corresponding central intensity profile in Fig. 2(d) shows a flat distribution around the ideal image point, which infers a superior enhancement on focus latitude than that from a finite-width annular aperture. Since the flat distribution comes from the equilibrium of the descending term $f_{(10)}f_{11}$ and ascending terms $f_{00}f_{(10)}$ and $f_{00}f_{11}$, the enhancement mechanism is no longer valid when the cosine function $f_{00}f_{11}$ starts to descend after propagating a half period from the focal point. This indicates the maximum extent of constant intensity can be represented by the minimum period of these cosine functions. With reference to Figs. 2(c) and 2(d), the cosine function with minimum period results from the interference between the innermost diffraction order $(0,0)$ and the outermost diffraction order $(\pm 1,\pm 1)$. The period of the cosine function $f_{00}f_{11}$ can be regarded as an accurate metric to evaluate the extent of focal range, which has the form

$$\text{DOF} \approx \frac{\lambda}{1 - \sqrt{1 - 2(\lambda/p)^2}} = \frac{\lambda}{1 - \sqrt{1 - (\sqrt{2}\lambda/p)^2}}$$

$$= \frac{\lambda}{1 - \sqrt{1 - \text{NA}_{\text{eff}}^2}}. \tag{5}$$

Here NA_{eff} represents the effective NA at which the outermost diffraction orders locate. In fact, each cosine function, in Eq. (3) can be regarded as the two-beam interference pattern from a pair of diffraction orders at the pupil. Equation (5) indicates that the focus latitude enhancement by a phase-shifted central order is related to the minimum period of the destructive interference patterns.

III. REALIZING THE MECHANISM BY PHASE-SHIFTING MASK

Figure 3 shows two symmetrical phase mask designs for contact hole patterning: outrigger type[15] and rim type.[16] By properly arranging the dimension and location of the assist features, the low frequency components at the center of the pupil are phase shifted by π, which satisfies the requirement for focus latitude enhancement as mentioned previously. Note the spectrum energy is concentrated around the center and edges of the pupil. This confirms that the coarse nine-point mesh in the pupil plane can evenly sample the most significant characteristics of Fourier spectrum to approximate the defocus behavior correctly. The reconstructed images have narrow, bright central spots with side-rings revolving around, which indicate the resolution capability to print a deep submicron contact hole using 248 nm exposure tools.

Since the contact mask designs in Fig. 3 are composed of several rectangular apertures with different phase angle and transmission, their Fourier spectrum at the pupil can be de-
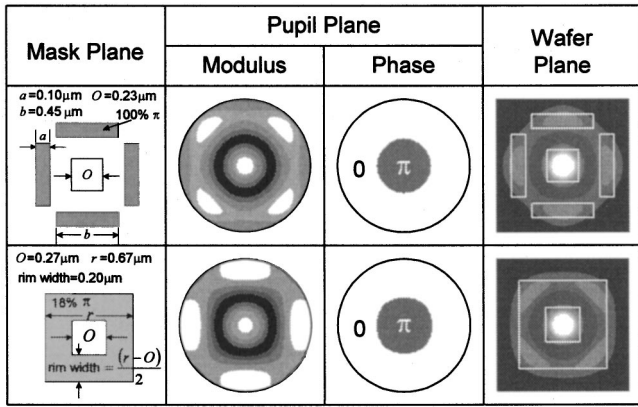
FIG. 3. Symmetrical phase mask designs for focus latitude enhancement. The low frequency components in the Fourier spectrum are phase shifted by π. The reconstructed images have a narrow, bright central lobe with a sidering revolving around.

scribed in an analytical form by the operation of shifting and addition properties of Fourier transform. For the outrigger design in a Levenson-type PSM, its Fourier spectrum, apart from a constant factor for energy conservation, is described by

$$f(\sigma_x, \sigma_y) = O^2 \ \mathrm{sinc}(O\sigma_x)\mathrm{sinc}(O\sigma_y) - 2ab$$
$$\times \cos(c\sigma_x)\mathrm{sinc}(a\sigma_x)\mathrm{sinc}(b\sigma_y) - 2ab$$
$$\times \cos(c\sigma_y)\mathrm{sinc}(b\sigma_x)\mathrm{sinc}(a\sigma_y). \tag{6}$$

Here O is the width of the main feature opening; a, b, and c are geometrical parameters of the outrigger related to the width, length, and separation from the main contact feature, respectively. Similarly, the Fourier spectrum of a rim-type contact with intensity transmittance t is described by

$$f(\sigma_x, \sigma_y) = O^2 \ \mathrm{sinc}(O\sigma_x)\mathrm{sinc}(O\sigma_y)$$
$$- \sqrt{t}r^2 \ \mathrm{sinc}(r\sigma_x)\mathrm{sinc}(r\sigma_y)$$
$$+ \sqrt{t}O^2 \ \mathrm{sinc}(O\sigma_x)\mathrm{sinc}(O\sigma_y). \tag{7}$$

The dimension criterion to achieve the phase inversion of a "zero-frequency" component can be decided by Eqs. (6) and (7). For the rim-type design, the rim width should obey the following rule to achieve the phase-shifting effect:

$$\mathrm{rim \ width} = \frac{r - O}{2} \geqslant \frac{O}{2}\left[\left(\frac{1 + \sqrt{t}}{\sqrt{t}}\right)^{1/2} - 1\right]. \tag{8}$$

Figure 4 shows the variation of amplitude profile at the pupil and the related intensity distributions of images with respect to the different width of the assist feature under the optical condition of 248 nm wavelength and a 0.55 NA projection lens. For the rim-type contact design with a 0.27 μm (0.6 λ/NA) contact window, the low frequency components at the center of the pupil almost diminish as a 0.11 μm rim width is assigned. Since the attenuation of low frequency components relatively emphasizes the high frequency components at the periphery of the pupil, the resulting image has a narrower central lobe than that without rim assignment [see
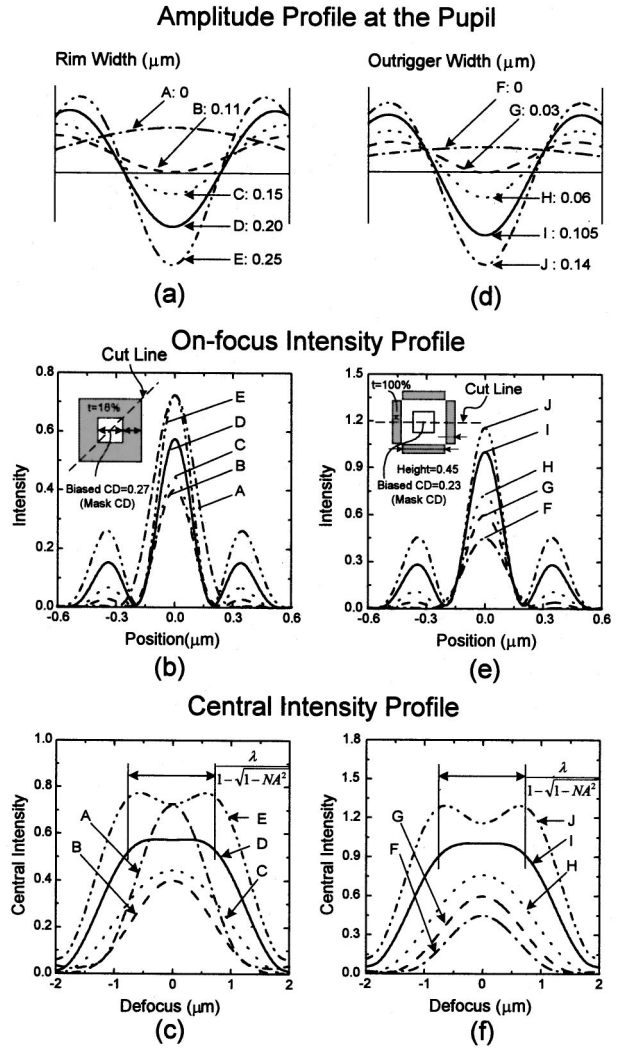

FIG. 4. Variation of amplitude profile at the pupil, on-focus image distribution, and central intensity distribution with respect to different assist feature sizes. The optical condition for simulation is a 0.55 NA projection lens and 248 nm wavelength.

Fig. 4(b)]. Its central intensity profile in Fig. 4(c) has a gentler variation as defocus, which implies a slight improvement on focus latitude. This is because the amplitude distribution at the pupil is analogous to a grayscale annular pupil filter. As the rim width further increases to exceed the dimension criterion of Eq. (8), the amplitude of the zero-frequency component is intensified but phase shifted by π. Simulation results in Figs. 4(b) and 4(c) show larger side-lobe intensity and a flatter central intensity profile following the enhancement of phase-shifted low spatial frequencies. Therefore the rim width should be properly adjusted to maximize the focus latitude enhancement while restraining the side-lobe intensity from resist surface erosions. Figure 4(c) shows that a 0.20 μm rim width is an optimum design to provide the flattest intensity distribution around the ideal image point. When the rim width is over this optimum value, the central intensity is neither monotonic decreasing nor remaining con-

stant but curves up in the vicinity of the focal point. Referring to Fig. 2(d), this anomalous distribution can be easily comprehended in the nine-beam interference case if we increase the magnitude of the phase-shifted central order so that the effect of the ascending terms $f_{00}f_{(10)}$ and $f_{00}f_{11}$ outweighs that of the descending term $f_{(10)}f_{11}$. Consequently, the curving-up characteristic is ascribed to the overemphasis of the phase-shifted low frequency components at the center of the pupil. Figures 4(d)–4(f) show that the increase of the outrigger width has a similar effect on the resolution improvement and focus latitude enhancement.

In Sec. II, the extent of focus latitude from the phase-shifting method can be accurately approximated as the minimum period of destructive two-beam interference patterns. Since the diffraction pattern of an isolated hole fills the entire pupil and its energy is concentrated at the center and periphery of the pupil, the estimated DOF of Eq. (5) should be modified by replacing the effective NA with a full lens NA, which has the form

$$\text{DOF} \approx \frac{\lambda}{1 - \sqrt{1 - NA^2}}. \tag{9}$$

Simulation data in Figs. 4(c) and 4(f) demonstrate the validity of Eq. (9). This equation indicates that the capability of focus latitude enhancement using a symmetric phase mask design depends on the optical system parameters (wavelength and projection-lens NA) only.

IV. ISSUES FOR PRACTICAL APPLICATIONS

A. Effect of illumination angle

In previous discussions, the aerial image was considered under coherent illumination to simplify the analysis of optical behavior. However, a wafer stepper adopts partially coherent illumination by a source of finite extent because coherent illumination implies an on-axis point source with zero intensity for exposure. Partially coherent illumination includes a range of incident angles on the mask, both on axis and off axis. According to the Abbe method of imaging, the image from a source of finite extent is the incoherent sum of the coherent image from every point on the sources. Hence, it is important to understand the effect of the illumination angle on the focus latitude enhancement for actual process optimization.

As explained in Sec. II, the focus latitude enhancement under coherent (on-axis) illumination comes from the destructive interference of the negative low frequency components at the center of the pupil and the positive high-frequency components near the edge. In Fig. 5(a) we examine the two-beam interference pattern of the negative innermost Fourier component (f_0) and positive outermost one (f_1) along the optical axis direction to elucidate the influence of oblique illumination because most of the spectrum energy is concentrated around these two spatial frequencies. When the mask is illuminated by an off-axis point source, the diffraction pattern is shifted off optical axis so that these two spatial frequencies are distributed on alternated sides of
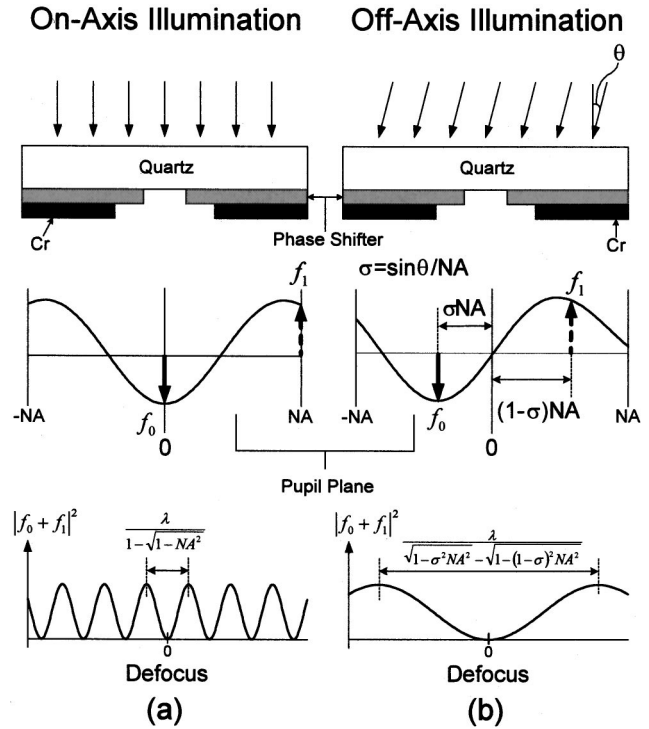

FIG. 5. Effect of illumination angle on the amplitude profile at the pupil under (a) on-axis illumination and (b) off-axis illumination. The interference pattern of f_0 and f_1 under on-axis illumination is rapidly upward to compensate intensity as defocus, while that under off-axis illumination behaves as a slowly varying function of defocus.

the axis [Fig. 5(b)]. The two-beam interference pattern has a cosinusoidal distribution with a period described in the form

$$\text{period} = \frac{\lambda}{\left| \sqrt{1 - \sigma^2 NA^2} - \sqrt{1 - (1-\sigma)^2 NA^2} \right|}, \tag{10}$$

where σ denotes the ratio of the sine of illumination angle to the projection lens NA. For on-axis illumination ($\sigma=0$), Eq. (10) reduces to Eq. (9), and the destructive interference pattern is exactly the $f_{00}f_{11}$ term in Fig. 2(d), which is utilized to counterbalance the intensity loss as defocus. For off-axis illumination, since f_0 and f_1 are on alternated sides of the axis, their radial distances become approximate so that the period of the interference pattern is dramatically increased. Hence the destructive interference pattern behaves as a slowly varying function of defocus. This is reminiscent of the principle of off-axis illumination for the DOF enhancement of a dense pattern formed by a few diffraction orders. However, the image reconstruction of sparse patterns encounters a multiple-beam interference that both constructive interference and destructive interference are included in the image formation. Since enlarging the period of destructive interference, a larger illumination angle would dilute the phase-shifting effect for focus latitude enhancement of sparse hole patterns.

Figure 6 shows the variation of the central intensity profile with respect to the obliqueness of illumination. The shape of the illuminator is arranged to a ring for the symmetry of image formation. The mask condition for simulation is
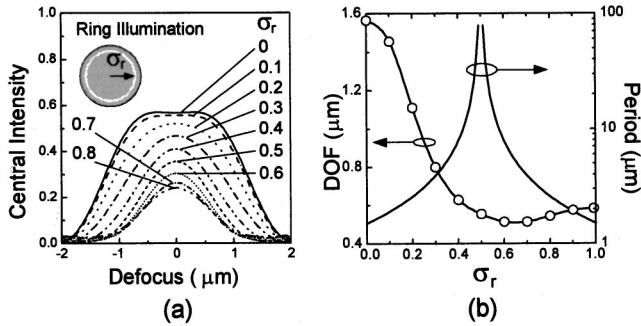
FIG. 6. (a) Central intensity profile under ring illumination with different radius σ_r. (b) The dependence of DOF for 10% intensity loss on σ_r. The pattern size is 0.27 μm with a 0.20 μm rim width.

the same as the optimum design of rim-type contact in Fig. 4(c) with the flattest central intensity profile under coherent illumination. In Fig. 6(a) the flat intensity profile becomes rounded as the illumination angle increases. We convert the central intensity distribution in Fig. 6(a) to DOF in Fig. 6(b) by the definition of 10% tolerance of on-focus intensity loss. Equation (10) is also plotted in this figure in log scale to verify our explanation in the above paragraph. It shows the DOF is drastically reduced as the illumination angle σ_r increases from 0 to 0.5. Although the period decreases again as σ_r further increases from 0.5 to 1.0, only a negligible amount of DOF enhancement is observed. This is because a large illumination angle makes the distribution of spatial frequencies at the pupil so asymmetric that the destructive interference possesses a much smaller amount of intensity compared with that of constructive interference.

The influence of increasing illumination angle on the central intensity profile in Fig. 6(a) is similar to that by reducing the size of assist features [Figs. 4(c) and 4(f)]. Intuitively, we may increase the size of assist features to compensate DOF as partially coherent illumination is applied. Under conventional disk illumination with a partial coherent factor of 0.3, the simulation results in Fig. 7(a) show that a 0.25 μm rim width has a flat central intensity profile, which is similar to that of a 0.20 μm rim width under coherent illumination in Fig. 6(a). We decompose the disk illumination into a ring
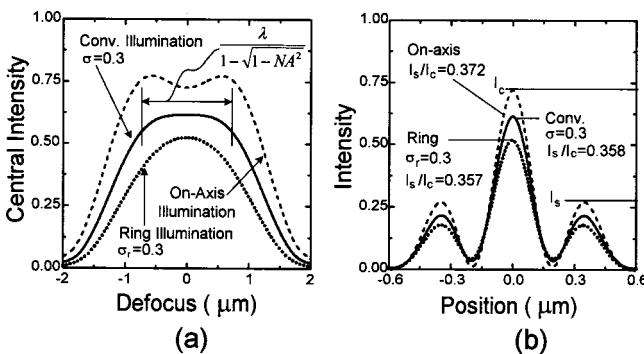

FIG. 7. (a) Central intensity profile of an isolated contact hole under different illumination conditions. (b) The corresponding on-focus intensity profile in the diagonal direction of rim-type mask contact. The pattern size is 0.27 μm with a 0.25 μm rim width.

illumination with purely off-axis light fluxes and on-axis illumination to elucidate the mechanism of DOF enhancement under partially coherent illumination. For on-axis illumination, an excess rim width overemphasizes the destructive interference so that its central intensity profile has the curving-up characteristic in the vicinity of the ideal image point. On the other hand, the central intensity under ring illumination with radius σ_r of 0.3 declines monotonically as defocus because a larger illumination angle dilutes the phase-shifting effect. Therefore, as disk illumination is applied, the intensity distributions from on-axis and off-axis illumination are averaged out so that a range of constant intensity is obtained again. Figure 7(b) shows the corresponding on-focus image profiles under the three illumination conditions in Fig. 7(a). The simulation results indicate that a larger illumination angle diminishes the image sharpness but keeps the ratio of side-lobe intensity to central-lobe intensity almost invariant. Therefore, although an excess rim width can regain the focus latitude enhancement under partially coherent illumination, the enhancement of side-lobe intensity should be taken into account to avoid undesired dimple formation on the resist surface.

B. Minimum pitch restriction

The foregoing discussion was focused on the performance of isolated contact-hole printing. However, the phase-shifting method should be capable of improving the focus latitude of high-density patterns to meet the real fabrication requirement. Figure 8(a) is the coherent imaging result of a square hole array with a pitch of $\sqrt{2}\lambda/\text{NA}$ in the mask plane. Its Fourier spectrum at the pupil is the replica of Fig. 2(c) except the $(\pm1,\pm1)$ order beams are just at the edge of the pupil. In this nine-beam interference condition, the central-lobe intensity is stronger than the side-lobe intensity in the range of constant axis intensity distribution. The mask pattern can successfully transfer to the photoresist if the threshold intensity for developing is sufficiently high to prevent side-lobe printing. When the pitch is smaller than $\sqrt{2}\lambda/\text{NA}$, the four $(\pm1,\pm1)$ order beams fall outside the pupil so that the image reconstruction changes from nine-beam interference to a five-beam case [Fig. 8(b)]. According to Eq. (4), when the $(\pm1,\pm1)$ order beams are cut off by the NA of a projection lens, the cosine terms with coefficients $f_{(10)}f_{11}$ and $f_{00}f_{11}$ vanishes and only the $f_{00}f_{(10)}$ term subsists. Since a single cosine term cannot maintain a constant central intensity with defocus, the mechanism for DOF enhancement fails. What is worse, the side-lobe intensity exceeds the central-lobe intensity so that the pattern transfer is incorrect. Therefore the coherent limit of array pitch can be expressed as

$$p_{\min} = \sqrt{2}\,\frac{\lambda}{\text{NA}}. \tag{11}$$

Figure 9 shows the dependence of DOF on the pattern pitch for an 18% transmission rim-type attenuated PSM under highly coherent illumination ($\sigma=0.3$). We manipulate the rim width to control the ratio of maximum side-lobe intensity
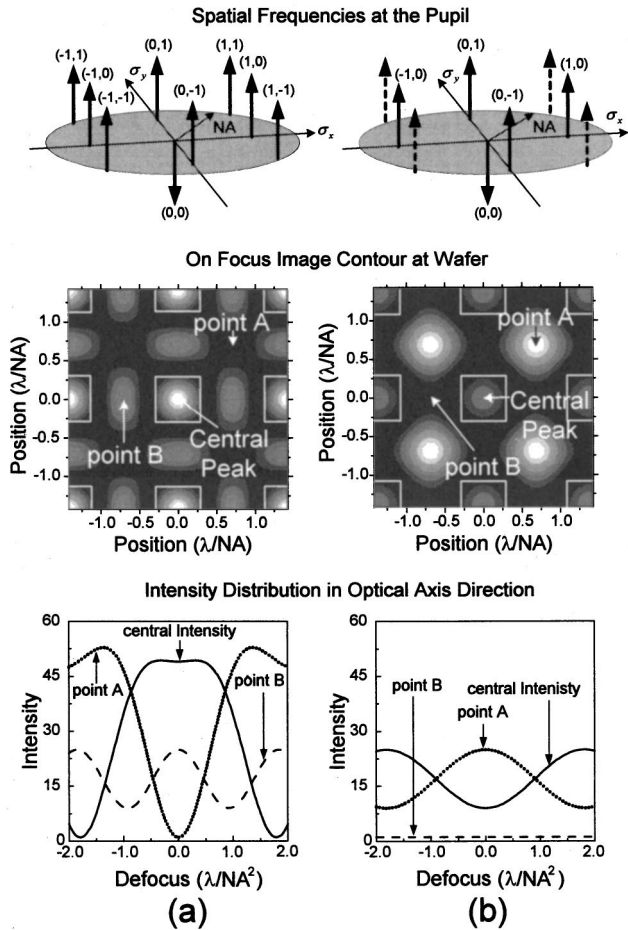
FIG. 8. Comparison of the imaging characteristics between (a) nine-beam interference and (b) five-beam interference with a π-phase-shifted zeroth-order diffraction beam.

(I_s) to central-lobe intensity (I_c) to monitor the side-lobe printability and examine the impact of optical proximity effect (OPE) on DOF. Since the highly coherent illumination spreads the diffraction beams at the pupil in a small range of angles, insufficient $(\pm1,\pm1)$ order beams are captured by the lens to provide a stronger $f_{(10)}f_{11}$ term as the pattern pitch is
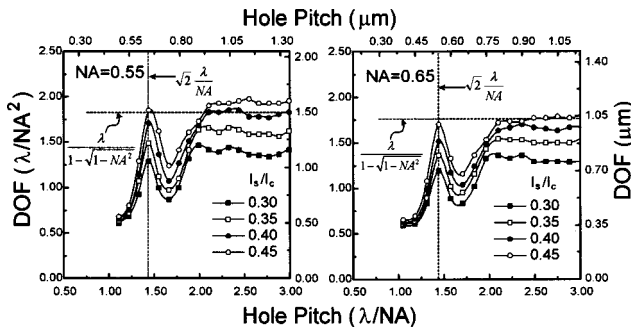

FIG. 9. Dependence of DOF for 10% on-focus intensity loss on the array pitch. The contact opening on mask is 0.6 λ/NA with different rim width to keep the ratio of side-lobe intensity to central-lobe intensity constant (σ =0.3).

smaller than $\sqrt{2}\lambda$/NA. To avoid side-lobe printing at the cross space of the contact array, the rim width should be much reduced to suppress the phase-shifting effect. Hence the DOF declines drastically as the pattern pitch is smaller than $\sqrt{2}\lambda$/NA. For a pitch between 1.4 and 2.0 λ/NA, although the multiple-beam-interference condition is satisfied, the DOF improvement is not as significant as we expected and reaches a local minimum at a pitch of 1.70 λ/NA. This is because the interference of the secondary peaks of each hole enhances the side-lobe intensity of a hole array.[17,18] Thus OPE limits the focus latitude enhancement under consideration to side-lobe printability. For a pitch larger than 2.0 λ/NA, the contact patterns are sparse enough that the interference from neighboring contact features only results in a small amount of DOF fluctuation.

Figure 9 also demonstrates that Eqs. (9) and (11) could be regarded as the performance guidelines of contact-hole printing using the symmetrical phase mask design with highly coherent illumination. The trade-off between DOF and minimum applicable pitch suggests that the NA is the most important parameter to determine the lithographic performance of this superresolution technique in fixed-wavelength lithography.

C. Influence of spherical aberration

A lens is seldom free from aberration. The primary lens aberration to affect the defocus behavior is spherical aberration. To simplify the analysis, we assume the aberration resided in the projection lens is purely spherical. Since the phase deviation from spherical aberration is rotationally symmetric about the optical axis and depends on the radial distance only, the modified expression of central intensity is analogous to Eq. (3) except for an additional phase term in every cosine function, which has the form

$$I_c(d) = \sum_{m,n=0}^{\sqrt{m^2+n^2}\leqslant p\cdot NA/\lambda} \sum_{u,v=0}^{\sqrt{u^2+v^2}\leqslant p\cdot NA/\lambda} \alpha'_{mnuv} f_{mn} f_{uv}$$

$$\times \cos\{2\pi[(d/\lambda)(\sqrt{1-(m^2+n^2)(\lambda/p)^2}$$

$$-\sqrt{1-(u^2+v^2)(\lambda/p)^2}) + (w_{mn}-w_{uv})/\lambda]\}, \quad (12)$$

where

$$w_{mn} = w(\rho_{mn}), \quad \text{and} \quad \rho_{mn} = \frac{\sqrt{(m^2+n^2)(\lambda/p)^2}}{NA}.$$

Here w represents the aberration function and ρ denotes the pupil radius normalized by the NA of the projection lens. Since the spherical aberration in a great many optical systems is almost entirely fourth-order wave aberration (third-order ray aberration), we assume the aberration function w in the projection system has the form of a Zernike spherical aberration.[19] Figure 10 shows the three-dimensional plot of a Zernike spherical aberration as pupil wave front deformation. It is shown that a coarse nine-point mesh can evenly sample the prominent characteristics of this rotational-
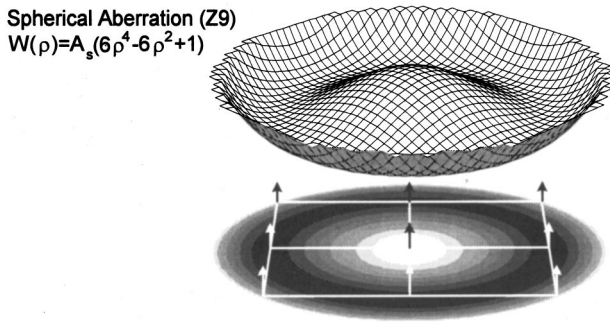
FIG. 10. Shape of Zernike spherical aberration (Z9) plotted as pupil wave-front aberration. The contour map drawn beneath the three-dimensional plot shows that a coarse nine-point mesh can sample the most significant deformations of this aberration.

FIG. 12. Dependence of (a) best focus position and (b) DOF on rim width of an 18% transmission attenuated PSM under the influence of spherical aberration. The mask CD is 0.27 μm. The minimum rim width to shift the phase of the zeroth-order frequency is 0.112 μm. ($\lambda=248$ nm, NA=0.55, and $\sigma=0.3$).

symmetry aberration. Hence the nine-beam interference can be utilized again for a clear visualization of the influence of spherical aberration on defocus behavior.

Figure 11(a) corresponds to the case of a binary intensity mask in which all the diffraction components at the pupil are in phase. Let a tiny amount of spherical aberration with a coefficient A_s of 0.02λ reside in the pupil plane. Since the spherical aberration shifts the cosine terms $f_{00}f_{(10)}$ and $f_{(10)}f_{11}$ to opposite defocus directions, the intensity variation of the image near focus is smeared and the best focus shift is inconspicuous. On the other hand, the same amount of spherical aberration results in a quite asymmetric central intensity distribution as the zeroth-order beam is phase-shifted by π [Fig. 11(b)]. This is because the split distribution of destructive cosine term $f_{00}f_{(10)}$ and the constructive cosine term $f_{(10)}f_{11}$ alters the equilibrium of the central intensity distribution. The diffraction focus, which stands for the defocus point with maximum irradiance, is significantly deviated from the ideal image point. In addition to the focus shift, the asymmetric central intensity profile also reveals the degradation of DOF. The above analysis suggests that the PSM method is apt to be influenced by spherical aberration rather than the conventional Cr mask.

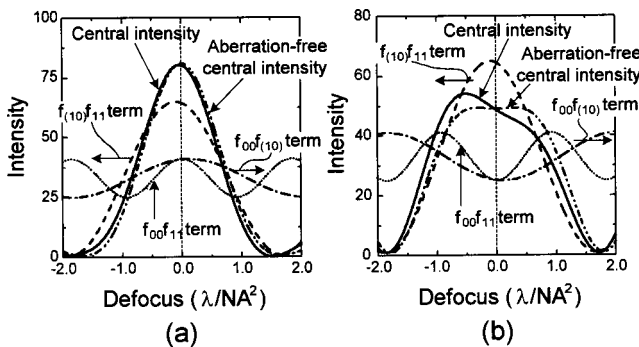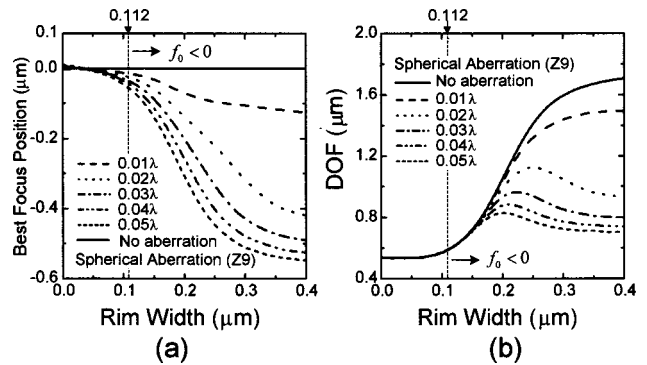Figure 12 shows the dependence of the best focus position and DOF on the rim width with a varying amount of spherical aberration. The simulated DOF is the focus range to allow 10% loss of central intensity at diffraction focus, and the best focus position is defined by the midpoint of the DOF. In the absence of spherical aberration, the DOF is significantly improved when the rim width exceeds the dimension criterion of Eq. (8) to shift the phase of the zeroth-order beam by π. However, the presence of a spherical aberration results in an obvious focus shift for the rim width larger than the dimension criterion. Increasing the amounts of spherical aberration exacerbates the focus shift and degrades the DOF enhancement. For an aberration coefficient larger than 0.02λ, a large rim width instead leads to DOF degradation. This is because a larger rim width enhances the destructive interference so that the asymmetry of central intensity distribution due to the misalignment of the constructive and destructive interference pattern is further deteriorated to cause a smaller DOF. No significant focus position variation and DOF degradation are observed for a small rim width with a positive zeroth-order beam. The simulation results show good agreement with our inference by the nine-beam interference in Fig. 11.

V. PRINTING EXPERIMENTS

A. CD-defocus characteristics of 0.17 μm contact-hole printing

To corroborate our analysis in the previous sections we investigate the printing characteristics of 0.17 μm contact holes, which correspond to a low $k1$ value of 0.38 to access the resolution limit of our exposure system. A $5\times$ KrF stepper with a NA of 0.55 and maximum σ of 0.8 was used in this evaluation. A 0.5-μm-thick chemically amplified resist was spin coated on a 200 mm wafer with a stack of 0.8-μm-thick undoped silicon glass (USG) and an antireflection coating layer on silicon substrate. A rim-type attenuated PSM consisting of MoSi single-layer shifters with transmittance of 18.9% and averaged phase angle of 181.3° at 248 nm wavelength was adopted in our experiments. Features for evaluation include a variety of hole arrays whose matrix is 7×7 with different pitches. The mask CD was measured using
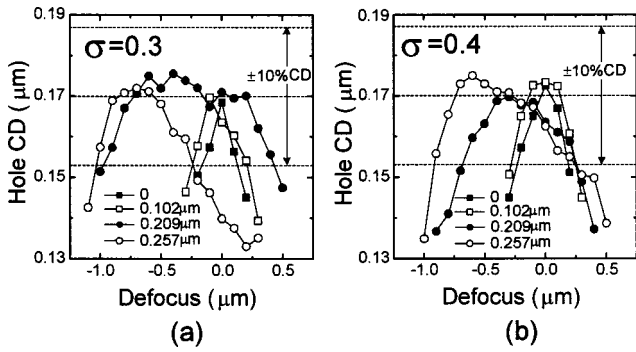

FIG. 11. Influence of spherical aberration on the central intensity distribution of nine-beam imagine for (a) all diffraction orders in phase and (b) zeroth order 180° out of phase. The aberration coefficient A_s is 0.02λ.

FIG. 13. CD-defocus curves of an isolated 0.17 μm contact hole with four different rim widths (18.9% transmittance): (a) illumination cohernece σ=0.3 and (b) σ=0.4. The mask CD is 0.279 μm (0.62 λ/NA).

Holon EMU-200A SEM. All wafer CD measurements were done using a Hitachi S8820 in-line CD SEM.

Figure 13 shows the experimental CD-defocus curves of a 0.17 μm isolated contact with different rim width assignment. Compared with the zero rim-width condition (Cr mask case), a 0.102 μm rim width slightly enhances the focus latitude but keeps the best focus position almost invariant. This is because the rim width is not large enough to shift the phase of the zero-frequency component at the pupil. With σ=0.3, a 0.209 μm rim width results in a large DOF of about 1.5 μm with the best focus position at −0.3 μm defocus [see Fig. 13(a)]. As the rim width further increases to 0.257 μm, the DOF degrades to 0.6 μm with an unacceptable best focus position at −0.7 μm. As explained in Sec. IV, this anomalous CD-defocus characteristic is ascribed to the asymmetric central intensity distribution due to spherical aberration. As we increase the partial coherence of illumination from 0.3 to 0.4, the DOF of a 0.209 μm rim width is decreased from 1.5 to 0.9 μm [see Fig. 13(b)]. However, the DOF of the 0.257 μm rim width is increased from 0.6 to 1.2 μm and its best focus position is moved from −0.7 to −0.3 μm defocus. According to the explanation in Sec. IV, increasing the illumination angle dilutes the influence of destructive interference. This implies that a larger illumination angle can abate the asymmetry of central intensity distribution due to the split distribution of constructive and destructive interference patterns caused by spherical aberration. Hence increasing the degree of partial coherence to introduce more off-axis light fluxes can alleviate the best focus shift. In addition, the more symmetrical intensity distribution regains some extent of DOF enhancement. This is why a 0.257 μm rim width shows better DOF performance under illumination coherence of 0.4 than that of 0.3. Consequently, the illumination condition and mask parameters (CD bias, rim width) should be carefully optimized to maximize the focus latitude enhancement while minimize the best focus shift in the presence of spherical aberration.

B. Dependence on hole pitch and illumination type

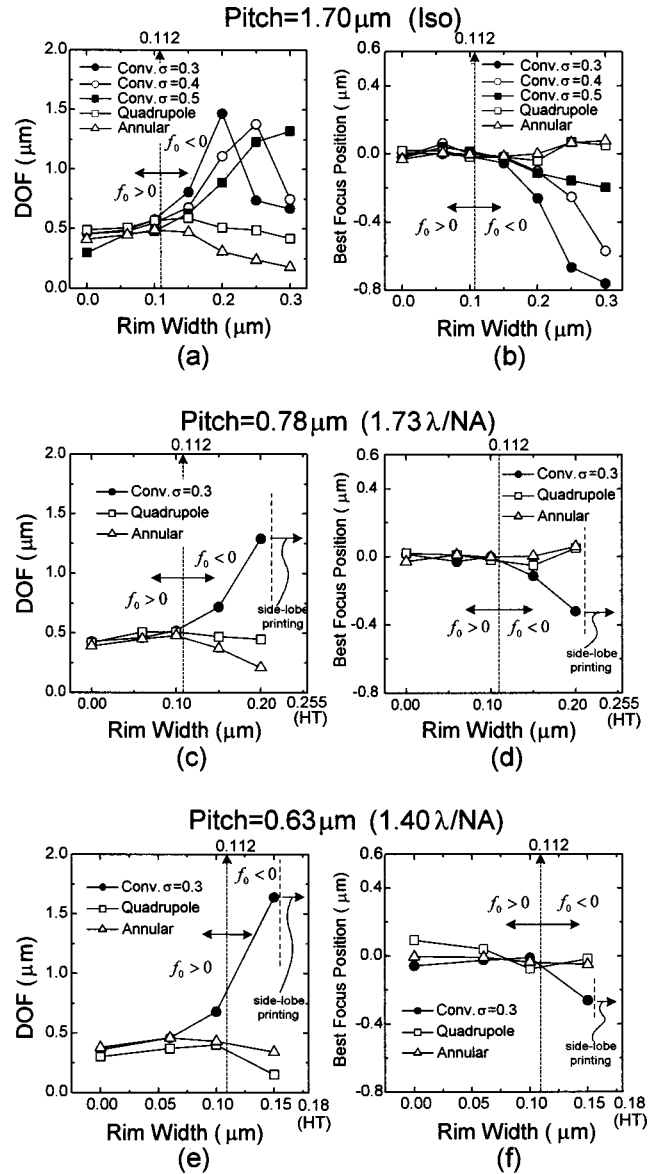Five hole array pitches were selected to represent iso, semi-iso, and dense hole patterns in our evaluation, including

FIG. 14. Dependence of experimental DOF and best focus position on rim width under different illumination conditions for 0.17 μm hole printing with a pitch greater than and equal to 1.4 λ/NA. The designed mask CD is 0.27 μm (0.6 λ/NA).

1.70 μm (3.87 λ/NA), 0.78 μm (1.73 λ/NA), 0.63 μm (1.40 λ/NA), 0.54 μm (1.20 λ/NA), and 0.45 μm (1.0 λ/NA). In addition to conventional disk illumination, quadrupole and annular illuminations composed of purely off-axis light fluxes were applied for comparison. The quadrupole scheme has square illumination poles located at the radius of 0.57 (σ) with an area of 0.33×0.33. The annular configuration has an inner radius of 0.4 and an outer radius of 0.8 (annular 1/2). The experimental DOF was extracted from exposure-defocus matrices at the definition of ±10% CD deviation and 5% exposure latitude. We categorized the five selected pitches into two groups according to the coherent pitch limit of the phase-shifting method ($\sqrt{2}\lambda$/NA≅1.4 λ/NA).

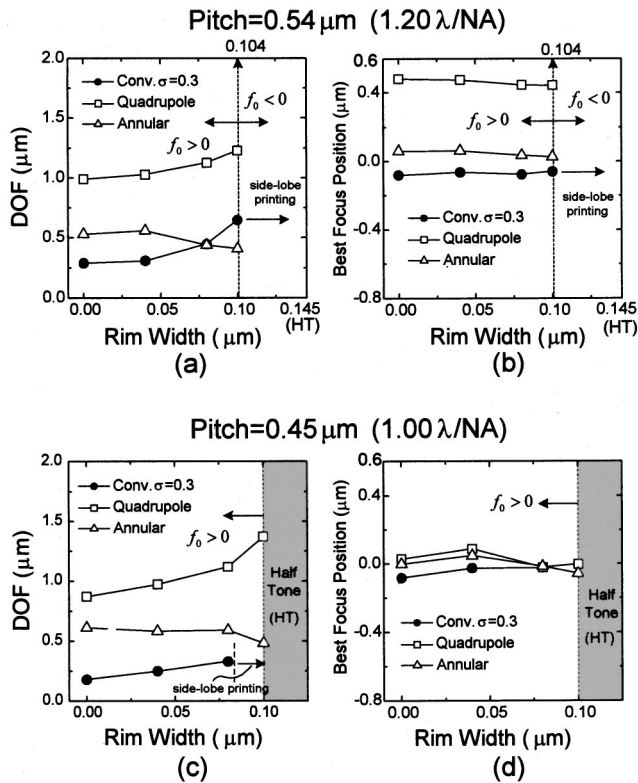Figure 14 shows the dependence of experimental DOF and best focus position on the rim width for array pitches

FIG. 15. Dependence of experimental DOF and best focus position on rim width under a different illumination condition for 0.17 μm hole printing with a pitch less than 1.4 λ/NA. The designed mask CD is 0.25 μm.

FIG. 16. Dependence of maximum experimental DOF and the related best focus position on the array pitch under different illumination conditions.

larger than 1.4 λ/NA. The pattern size on mask is 0.27 μm (0.6 λ/NA). The minimum rim width to shift the phase of the zeroth-order diffraction beam is 0.112 μm in the light of Eq. (8). For conventional illumination, the experimental DOF is effectively enlarged when the rim width is larger than 0.112 μm. However, the best focus shift is also exacerbated with increasing rim width. Figures 14(a) and 14(b) show that increasing the degree of partial coherence reduces the best focus shift at the expense of DOF. In comparison, the DOF by quadrupole and annular illuminations is slightly degraded as the rim width larger than 0.112 μm. No obvious focus variation is observed from these two purely off-axis illuminations. Note the hole pitch of 1.73 λ/NA, which corresponds to the critical pitch with a serious side-lobe printing problem due to OPE [see Fig. 9]; still a 1.3-μm DOF is achieved at a 0.20 μm rim width without side-lobe printing [see Fig. 14(c)].

Figure 15 shows the dependence of experimental DOF and best focus position on the rim width for array pitches smaller than 1.4 λ/NA. It is remarkable that the illumination type rather than the rim width dominates the focus latitude enhancement. This is because the rim width should be controlled within a small value to avoid the undesired side-lobe printing due to a negative zeroth-order diffraction beam. Unlike the phase-shifting method to enhance DOF by counterbalancing the constructive interference patterns and destructive interference patterns for multiple-beam imaging, the off-axis illumination enhances the focus latitude by relocating the diffraction beams at the pupil with equal radial distance
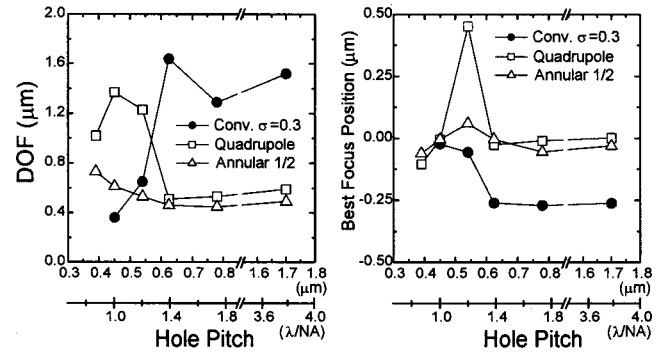
from optical axis, and thus applies to a dense pattern formed by a few diffraction orders. In Figs. 15(a) and 15(c), the quadrupole illumination shows superior DOF performance than other illumination schemes. However, this modified illumination also brings the side effect of best focus shift due to its specific utilization of a lens pupil at some particular pitches.[20,21] The best focus position of the 0.54 μm pitch by quadrupole illumination is dramatically shifted to 0.45 μm defocus [see Fig. 15(b)].

Figure 16 summarizes the experimental results in Fig. 14 and Fig. 15 by plotting the maximum experimental DOF and their corresponding best focus positions as a function of pitch. Under conventional illumination with σ=0.3, the phase-shifting method is effective in improving the DOF of hole patterns with a pitch larger than 1.4 λ/NA. The difference of best focus position between dense hole and sparse hole reaffirms the weak immunity of the phase-shifting method against spherical aberration. The experimental results also show that the quadrupole illumination and phase-shifting method are complementary to the dependence of DOF improvement on pattern pitches. Moreover, these two approaches have contrary distribution of best focus position variation through pitches. In the prospect of a larger iso/dense common process window, a customized illumination[22,23] combined with a phase-shifting method is worth developing for balanced DOF enhancement throughout all pattern pitches and suppresses the best focus shift from spherical aberration.

VI. CONCLUSION

The mechanism of focus latitude enhancement for hole imaging using symmetry phase-mask design is clearly understood by our simple coherent analysis that decomposes the defocus behavior into a sequence of cosine functions. The phase-shifting method improves the DOF by generating destructive interference to counterbalance the intensity loss as defocus. The DOF enlargement by this method is governed by wavelength and projection-lens NA. The extent of DOF can be correctively approximated by a simple formula [Eq. (9)]. Increasing the illumination angle would dull the DOF enhancement because the period of destructive interference

pattern (along axis direction) is enlarged so that its ability to offset the constructive interference is weakened. Since both constructive and destructive interference are required to generate a uniform intensity profile along axis direction, the hole pitch should be large enough to generate multiple-beam interference for hole imaging. In coherent illumination, this corresponds to at least nine diffraction beams taking part in the imaging, and thus hole pitch should be larger than $\sqrt{2}\lambda/NA$ for the application of a phase-shifting method. In addition, we found that the mechanism of a phase-shifting method to enhance DOF is also the reason why spherical aberration would cause severe focus shift and DOF degradation in attenuated PSMs than conventional masks.

We corroborate our analysis in KrF lithography using a rim-type attenuated PSM with 18.9% transmittance for 0.17 μm contact-hole printing. The experimental results show that the quadrupole illumination and symmetrical phase mask designs with highly coherent illumination are complementary to through-pitch DOF performance. With our thorough explanation of the mechanism of DOF enhancement, a rough performance guideline for deep submicron contact-hole patterning using symmetrical phase mask designs is established.

[1] M. D. Levenson, N. S. Viswanathan, and R. A. Simpson, IEEE Trans. Electron Devices **29**, 1828 (1982).

[2] T. Terasawa, N. Hasegawa, T. Kurosaki, and T. Tanaka Proc. SPIE **1088**, 25 (1989).

[3] H. Iwasaki, K. Hoshi, and H. Tanabe, Proc. SPIE **3412**, 601 (1998).

[4] R. J. Socha, X. Shi, K. Holmen, M. Dusa, W. Conley, J. S. Petersen, F. Chen, T. Laidig, K. Wampler, R. Caldwell, M. C. Chu, C. Su, K. Huang, C. Chen, F. Wang, C. Le, C. Pierrat, and B. Su, Proc. SPIE **3679**, 38 (1999).

[5] N. Kachwala, J. S. Petersen, and M. McCallum, Proc. SPIE **4000**, 1163 (2000).

[6] L. C. Choo, O. Park, M. J. Sack, and S. C. Tam, Proc. SPIE **4000**, 1193 (2000).

[7] F. Schellenberg, M. D. Levenson, and P. J. Brock, Proc. SPIE **1604**, 274 (1991).

[8] R. J. Socha, J. S. Petersen, F. Chen, T. Laidig, K. Wampler, and R. Caldwell, Proc. SPIE **3546**, 617 (1998).

[9] J. W. Goodman, *Introduction to Fourier Optics,* 2nd ed. (McGraw-Hill, San Francisco, 1996), Chap. 8.

[10] M. Mansuripur, *The Physical Principles of Magneto-optical Recording* (Cambridge University Press, Cambridge, England, 1995), Chap. 3.

[11] G. P. Tolstov, *Fourier Series* (Prentice-Hall, Englewood Cliffs, NJ, 1962), Chap. 7.

[12] J. Durnin, J. Opt. Soc. Am. A **4**, 651 (1987).

[13] G. Indebetouw, J. Opt. Soc. Am. A **6**, 150 (1989).

[14] H. Watanabe, Jpn. J. Appl. Phys., Part 1 **33**, 6831 (1994).

[15] T. Terasawa, N. Hasegawa, T. Tabata, S. Katagari, and T. Kurosaki, J. Vac. Sci. Technol. B **8**, 1300 (1990).

[16] Y. Yanagishita, N. Ishiwata, Y. Tabata, K. Nakagawa, and K. Shigematsu, Proc. SPIE **1463**, 207 (1991).

[17] A. Otaka, Y. Kawai, and T. Matsuda, Jpn. J. Appl. Phys., Part 1 **32**, 5880 (1993).

[18] H. Shimizu, F. Uesawa, T. Oda, and M. Sugawara, Jpn. J. Appl. Phys., Part 1 **34**, 6598 (1995).

[19] V. N. Mahajan, *Aberration Theory Made Simple* (SPIE Optical Engineering, Washington, 1991), Chap. 8.

[20] K. Tsujita, J. Sakai, A. Nakae, S. Nakao, and W. Wakamiya, Proc. SPIE **3334**, 855 (1998).

[21] S. Nakao, A. Nakae, J. Sakai, T. Miura, S. Tatsu, K. Tsujita, and W. Wakamiya, Jpn. J. Appl. Phys., Part 1 **37**, 5949 (1998).

[22] T. Ogawa, M. Uematsu, K. Takeuchi, A. Sekiguchi, and T. Oda, Proc. SPIE **2726**, 34 (1996).

[23] T. S. Gau, R. G. Liu, C. K. Chen, C. M. Lai, F.J. Liang, and C. C. Hsia, Proc. SPIE **4000**, 271 (2000).